Journal of ELECTRONIC MATERIALS, Vol. 38, No. 2, 2009
DOI: 10.1007/s11664-008-0595-0
© 2008 TMS
Special Issue Paper

Anisotropic Crystal Plasticity Finite Element Modeling of the Effect of Crystal Orientation and Solder Joint Geometry on Deformation after Temperature Change

A. ZAMIRI,[1] T.R. BIELER,[2,3] and F. POURBOGHRAT[1]

1.—Mechanical Engineering, Michigan State University, East Lansing, MI 48824-1226, USA. 2.—Chemical Engineering and Materials Science, Michigan State University, East Lansing, MI 48824-1226, USA. 3.—e-mail: bieler@egr.msu.edu

The crystal orientation of the tin phase in a Pb-free Sn solder joint has a significant effect on the stress state, and hence on the reliability of the solder joint. A set of crystal plasticity analyses was used to evaluate stress and strain resulting from a 165°C temperature change in a single-crystal joint using two simplified geometries used in practical solder joints. Phenomenological flow models for ten slip systems were estimated based upon semiquantitative information available in the literature, along with known anisotropic elastic property information. The results show that the internal energy of the system is a strong function of the tin crystal orientation and geometry of the solder joint. The internal energy (and presumably the likelihood of damage) is highest when the crystal *c*-axis lies in the plane of the substrate, leading to significant plastic deformation. When the *a*-axis is in the plane of the interface, deformation due to a 165°C temperature change is predominantly elastic. The texture of the copper substrate using isotropic Cu elastic properties, or anisotropic elastic properties with [001] ∥ substrate normal direction, does not have a significant effect on the stress or strain in the Sn phase of the joint.

Key words: Finite element, single crystal, tin, thermal expansion, anisotropy

INTRODUCTION

Due to environmental concerns about lead contamination, lead-free solder alloys are required in most electronic systems. To select a lead-free solder for a specific application, the solder's response to anticipated creep and thermomechanical fatigue (TMF) conditions needs to be anticipated.[1–18] The reliability of tin-based solders is often examined using phenomenological models.[19–23] Many studies examine the reliability of solder joints arising from evolution of intermetallic morphology in the interface.[24–29] In contrast to lead-tin-based solders, for which the probability of fracture is directly related to the strain amplitude, crystal orientations in initial tin-phase microstructure have a large impact on reliability of lead-free solders,[30–49] so damage can develop in any region of a package. To predict deformation during the TMF cycling of a solder joint, a deep knowledge of deformation mechanisms in Sn is required. The deformation of tin-based solders is due to operation of preferred slip systems.[40,48–51] The governing constitutive relationships have been investigated many times, e.g., Refs. 52–54, but the role of crystal orientation on deformation has been the primary focus much less frequently.[37–49] Assuming that intermetallic issues can eventually be controlled so that they do not dominate reliability concerns, the deformation in Sn will affect reliability, which is the focus of this paper.

Deformation usually results from thermal loads caused by the expansion mismatch between the

(Received April 20, 2008; accepted October 15, 2008; published online November 19, 2008)

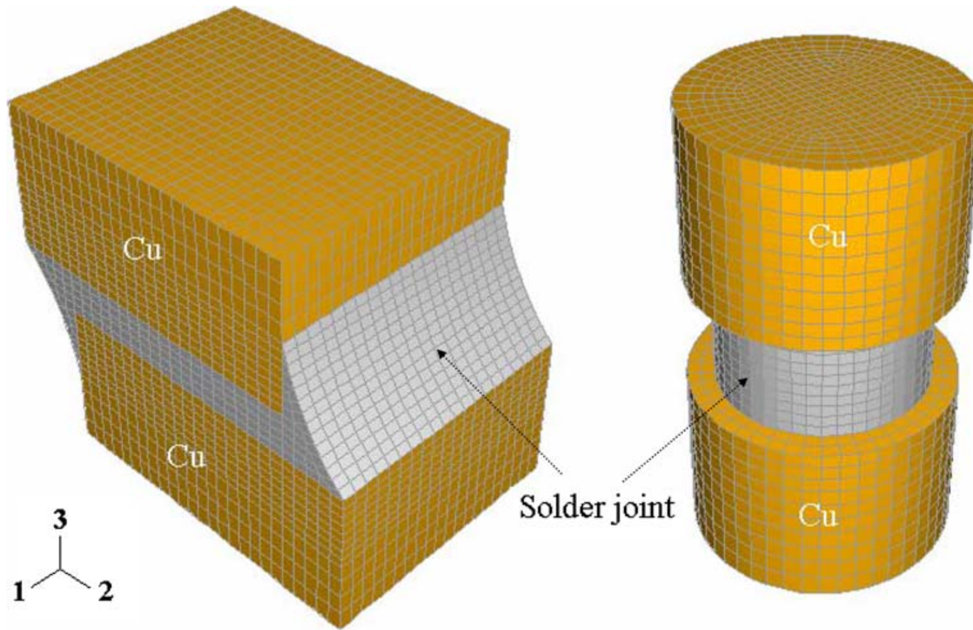

Fig. 1. The computational models used in these investigations: (a) the shear lap model that simulates the geometry of a surface mount capacitor or resistor, and (b) the cylindrical model which approximates a solder ball joint such as used in a ball grid array.

component, the tin, and the substrate (which often have thermal expansion properties close to those of copper) during the TMF cycling. Depending on the application, the TMF temperature variation can vary between −50°C to 150°C, for example, in automotive or aerospace engine settings, or from room temperature to 85°C in household electronics and computer applications. Such cycling can cause heterogeneous deformation that leads to crack nucleation, growth, and eventual failure of the system.[44,45,48,49]

Prior investigations show that the tin phase in lead-free solder joints is often a single crystal or a multicrystal, and there is a direct relationship between the damage nucleation and the crystal orientation.[46–49] In as-fabricated packages, 40% of the joints could be single crystals.[55] Some orientations are elastically more compliant or plastically softer with respect to the specified external loads, such that internal strain energy evolution during the TMF cycling can vary greatly from joint to joint.[47–49]

In this work an elastic–plastic anisotropic crystal plasticity model embedded in a commercial finite element code is used to analyze the total internal energy and plastic work that develops during a temperature change in tin-based solder joints with different single-crystal tin orientations. This approach has been used to investigate other non-cubic materials,[56–59] but only recently with Sn using only plastic deformation,[39] so this is a first attempt to use this approach using an anisotropic elastic–plastic deformation model. Also the effect of the copper orientation on the total internal energy of the solder joint is examined. The results of these analyses provide important insight into the Sn single-crystal orientations that are more likely to stimulate damage nucleation, and thus provide a physical basis for identifying reliability criteria arising from the Sn orientation in a solder joint.

SIMULATION DETAILS

Two geometries with different solder shapes were investigated in this work (Fig. 1). The geometry with a 1-mm square cross section is representative of a shear lap specimen geometry, which is similar to solder joints used in surface-mount components such as capacitors and resistors. The 1-mm-diameter cylindrical geometry is similar to solder joints used in ball attachments of packages. These two simplified geometries allow similarities and differences in the interaction between crystal orientation and attachment geometry to be explored.

In the elastic–plastic analysis, the whole model was heated up from −15°C to 150°C, with the simplifying assumption that the properties did not change with temperature,* and no other external loads were imposed. All the nodes on the bottom of the computational models were constrained not to move in the $Z(3)$ direction (Fig. 1). One node on the bottom corner of the shear lap model and one node on the bottom plane in the center of the cylindrical model were completely fixed. The tin-based solder was modeled to be anisotropic with the properties shown in Table I and illustrated in Fig. 2.[46–49,60,61]

*The variation of the thermal properties is known. The expansion coefficient anisotropy ratio is nearly independent of temperature, and the elastic anisotropy ratio increases with increasing temperature.

Table I. Elastic Constants (GPa) and Thermal Expansion Coefficients (ppm/°C) of Tin

C_{11}	C_{22}	C_{33}	C_{44}	C_{55}	C_{66}	C_{12}	C_{13}	C_{23}
72.3	72.3	88.4	22.0	22.0	24.0	59.4	35.8	35.8
α_{11}	α_{22}	α_{33}	-	-	-	-	-	-
16	16	31						

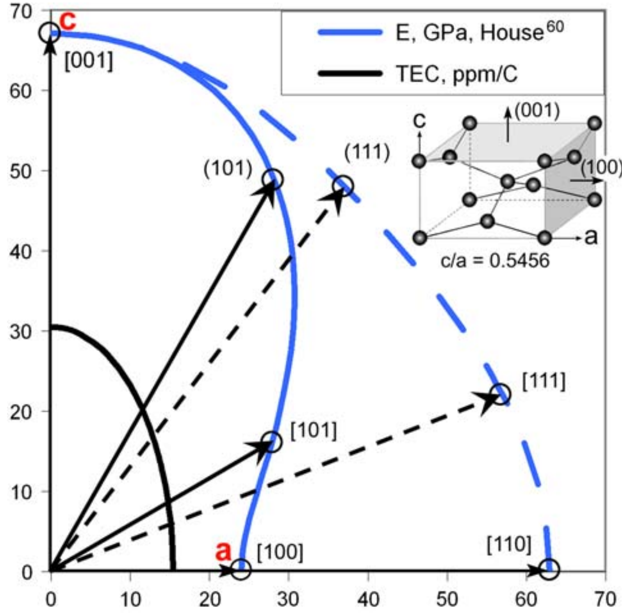

Fig. 2. For the tin unit cell (inset), the magnitude (with units indicated in the legend) of the expansion coefficient and Young's modulus is indicated by the distance from the origin to the curves. The expansion coefficient is isotropic only in the (001) plane, and Young's modulus is almost isotropic in the (101) and (10$\bar{1}$) planes.

The analyses were repeated for four different tin crystal orientations, as defined by Bunge Euler angles φ_1–Φ–φ_2: 0–0–0, which has the *c*-axis of the crystal perpendicular to the tin–copper interface, 0–90–0 and 90–90–0, in which the *c*-axis is parallel to the interface, and 0–45–0, in which the *c*-axis is tilted 45 deg with respect to the interface. To investigate the effects of the copper texture on the damage nucleation in the tin-based solder, two different properties for the copper substrate were considered; in one case the copper substrate was modeled as a single crystal having (001)[100] orientation with respect to the lab coordinate and with properties C_{11} = 178, C_{12} = 78.6, C_{44} = 45 (GPa), and $\alpha_{11} = \alpha_{22} = \alpha_{33}$ = 17.6 ppm/°C. In the other case, copper was isotropic with E = 136 GPa, ν = 0.33, and α = 17.6 ppm/°C. The copper substrate was considered to be fully elastic during the analysis.

A crystal plasticity model developed by Zamiri,[62] which is implemented into ABAQUS finite element software,[63] was used to analyze the elastic–plastic deformation in the tin phase. Using an optimization technique, Zamiri showed that during the plastic deformation of a single crystal the slip rate on any slip system could be expressed by

$$\dot{\gamma}^{\alpha} = \lambda \frac{\frac{\mathrm{sign}(\tau^{\alpha})}{\tau_y^{\alpha}} \exp\left[\frac{\rho}{m}\left(\frac{|\tau^{\alpha}|}{\tau_y^{\alpha}} - 1\right)\right]}{m \sum_{\beta=1}^{N} \exp\left[\frac{\rho}{m}\left(\frac{|\tau^{\beta}|}{\tau_y^{\beta}} - 1\right)\right]}, \tag{1}$$

where m and ρ are material parameters that control the shape of the single-crystal yield surface and it has been shown that they have a direct relationship with the stacking fault energy (SFE) of the material. For most materials m = 1 and ρ is obtained using the SFE of the material or experimental data. λ is a Lagrange multiplier which has been shown to be a measure of the rate of plastic work in a crystal, and τ^{α} and τ_y^{α} are the resolved shear stress and critical resolved shear stress for slip system α, respectively. Further details can be found in Ref. 62.

The relative activity of slip systems operating in tin has been examined by Fujiwara.[51] Based on this investigation along with other examinations of single-crystal deformation,[43,51] 32 slip systems were modeled, as indicated in Table II, ranked according to semiquantitative understanding of their likelihood to contribute to deformation.

Table II. Slip Systems in Tin, Ranked According to Their Presumed Activity

ID	Slip System	No. in Family
1	{100)<001]	2, most active
2	{110)<001]	2
3	{100)<010]	2
3	{110)<1$\bar{1}$1]/2	4 (like body-centered cubic metals)
5	{110)<1$\bar{1}$0]	2
6	{100)<011]	4
7	{001)<010]	2
8	{001)<110)	2
9	{011)<01$\bar{1}$]	4
10	{211)<01$\bar{1}$]	8, less active

{hkl)<uvw] recognizes tetragonal crystal symmetry (tin has a squashed diamond cubic structure).

Table III. Strain Hardening Parameters for Tin for Two Cases (h1 and h2) and for Different Slip System Sets Shown in Table II

Model	τ_0	τ_s	h_0	a	q	m	ρ
h1	20,21,…,29 for sets 1,2,…,10, respectively	30 for all	20 for all	2.0 for all	1.4 for all	1	80
h2	20 for sets 1–3	30 for all	40 for sets 1–3	2.0 for all	1.4 for all	1	80
	22 for sets 4–6		60 for sets 4–6				
	25 for sets 7–10		80 for sets 7–10				

The strain hardening model is expressed by the following hardening equation

$$\dot{\tau}_y^\alpha = \sum_{\beta=1}^{N} h^{\alpha\beta} |\dot{\gamma}^\beta|, \quad (2)$$

where $\dot{\gamma}^\beta$ is the plastic slip rate of the active slip system β, and $h^{\alpha\beta}$ denote the components of the hardening matrix. The $h^{\alpha\alpha}$ are known as self-hardening moduli, and $h^{\alpha\beta}$ for $(\alpha \neq \beta)$ are known as the latent-hardening moduli. A common type of hardening matrix is proposed as the following simple law[64–66]

$$h^{\alpha\beta} = h^\beta [q + (1-q)\delta^{\alpha\beta}] \quad \text{(no summation on } \beta\text{)}. \quad (3)$$

Here q is the so-called latent-hardening ratio, which is the ratio of the latent-hardening rate to the self-hardening rate of a slip system with values in the range of $1 < q < 1.4$. The parameter q can be considered as 1 for coplanar slip systems and 1.4 for non-coplanar slip systems. h^β is an evolutionary function denoting the self-hardening rate, which can be expressed as a function of either shear slips or resolved shear stress on slip systems. h^β is considered to evolve as

$$h^\beta = h_0 \left| 1 - \frac{\tau_y^\beta}{\tau_s} \right|^a \cdot \text{sign}\left(1 - \frac{\tau_y^\beta}{\tau_s}\right), \quad (4)$$

where h_0, a, and τ_s are slip system hardening parameters which are considered to be identical for all slip systems. h_0 denotes the initial hardening rate, τ_s the saturation value of the slip resistance, and a is the exponent describing the shape of the function.

Two different sets of strain hardening parameters were used to model the effect of the hardening behavior of tin on the analyses. Available single-crystal data is sparse and inconsistent among different research groups,[50,51] but the trends suggest that yield stresses are not as sensitive to crystal orientation as the hardening rates.[51] Consequently, model parameters are not fitted to any experimental data, and are thus best considered as thought experiments that examine the influence of plausible tin deformation characteristics. Hardening model h1 has a modest strain hardening characteristic that is the same for all slip systems, with the only difference being the initial yield stress. A slightly more realistic model (h2) reflects the observation that that the critical resolved shear stresses from single-crystal experiments often have similar values for different slip systems, but different hardening rates (or, as Fujiwara indicates,[51] different ability to cut through forest dislocations). These strain hardening parameters are shown in Table III.

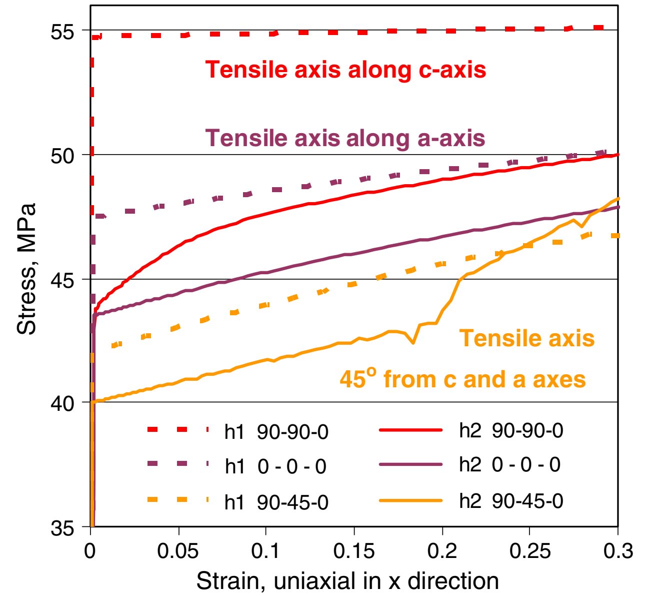

Fig. 3. Uniaxial stress–strain curves for two hardening cases using parameters in Table III for Bunge Euler angle tin orientations indicated in the legend.

The effects of these parameters are illustrated in Fig. 3, which shows how different hardening assumptions are reflected in uniaxial stress–strain behavior for three different crystal orientations. For this purpose, a single eight-node brick element with unit sides was used and uniaxially deformed along the specimen Z-axis using ABAQUS. The two faces of the cube normal to the loading axis are constrained to remain parallel to each other throughout the simulation to simulate a rigid testing machine. Uniaxial deformation is not typical for practical solder joints, but it is useful to illustrate effects of model parameters.

RESULTS AND DISCUSSION

Figure 3 shows the stress–strain curves for the uniaxial deformed tin grain in three different

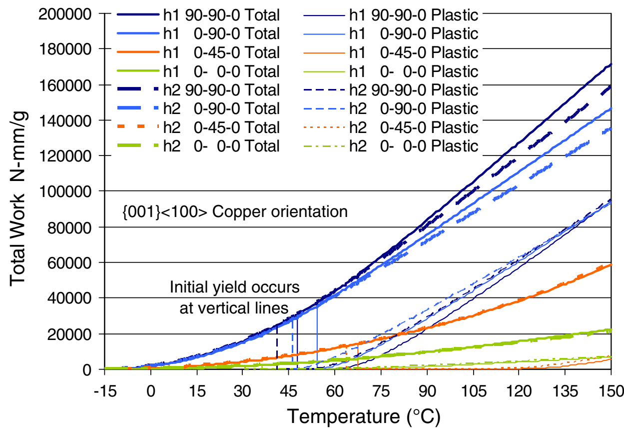

Fig. 4. Total internal strain energy increases with temperature for the fillet shear lap model with four different tin orientations and for two different strain hardening cases. Plastic energy dissipation starts where the vertical lines drop down from the total energy curves.

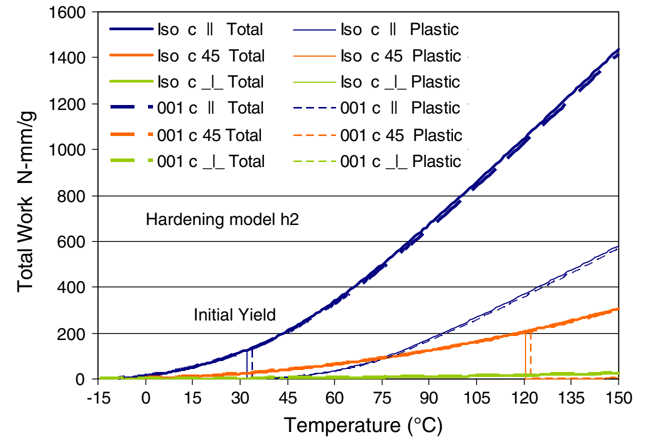

Fig. 5. Total internal energy increases with temperature for the cylindrical models for three different tin orientations, using isotropic copper or copper with (001)[100] orientation. The plastic energy dissipation starts where the vertical lines drop down from the total energy curves. No plastic deformation occurred for the *c* perpendicular substrate case.

directions: along the *c*-axis of the crystal (the hardest orientation), along the *a*-axis, and along a direction with the *c*-axis tilted 45 deg from the tensile axis that maximizes shear stress for a-slip on a (001) plane along the *a*-axis (the softest orientation). For the h1 case, the yield stresses are different from each other, and the hardening rate is lower when the yield stress is higher (because the saturation stress τ_s is the same). For the h2 case, the initial hardening rates (the slope of the curves) are higher, but the difference between the initial yield stress in different directions is smaller. These two strain hardening behaviors are used to compare the effects of strain hardening behavior on tin deformation in the solder joint.

Evolution of Internal Strain Energy

Figure 4 shows the change in internal strain energy (total work, thick lines) with respect to temperature (time step) for different tin orientations and hardening parameters using the shear lap geometry. The total work is the sum of elastic and plastic work, where the beginning of plastic work is indicated by fine vertical lines that identify the time step where the first element deformed plastically. The copper substrate was assumed to have {001}<100> orientation in these simulations. Clearly, the change in internal energy depends more on the tin-based solder joint orientation than strain hardening behavior. For both strain hardening cases, the internal energy is largest for the tin orientations that have the *c*-axis of the crystal parallel to the tin–copper interface [two cases are shown, with *c*-axis aligned with the shear lap longitudinal (0–90–0) and transverse (90–90–0) directions]. The strain energy is small when the *c*-axis of the crystal is normal to the interface (0–0–0). When the *c*-axis of the crystal is tilted 45 deg with respect to the interface normal (0–45–0), the amount of the internal energy is between the other two values.

Figure 5 shows the same internal energy calculation for the cylindrical model, showing a qualitatively similar result (differences will be discussed further below). For this geometry, the two hardening models differed similarly as in Fig. 4, so in Fig. 5, the hardening model h2 was used in the cylinder model, as it is closer to documented physical behavior,[51] and the copper texture in the substrate was varied between single-crystal and isotropic cases.

These results can be understood in terms of the anisotropic properties of single-crystal tin illustrated in Fig. 2, which shows that the coefficient of thermal expansion as well as the stiffness are smallest along the *a*-axes. The expansion coefficient of tin in the basal plane is isotropic, and nearly the same as that of copper, which exhibits isotropic expansion behavior. It is obvious from the geometry and the boundary conditions that tin is most constrained in the plane parallel to the interface while it is least constrained to expand or contract along a direction normal to the interface. Therefore, when the *c*-axis of the crystal is placed in a plane parallel to the interface it has the largest expansion mismatch, and thus generates the greatest internal strain energy in the system. If damage develops in proportion to the dissipated plastic energy in the system, then one may expect that the best tin orientation is 0–0–0, in which case the *c*-axis of the crystal is normal to the tin–copper interface; in this case, deformation in the substrate interface is only elastic.

The copper substrate on the electronic circuit boards can also have different textures, depending on the deposition process. Therefore, the texture of the copper may also influence the deformation in tin-based solder joints. To investigate this, the computational model with cylindrical geometry was

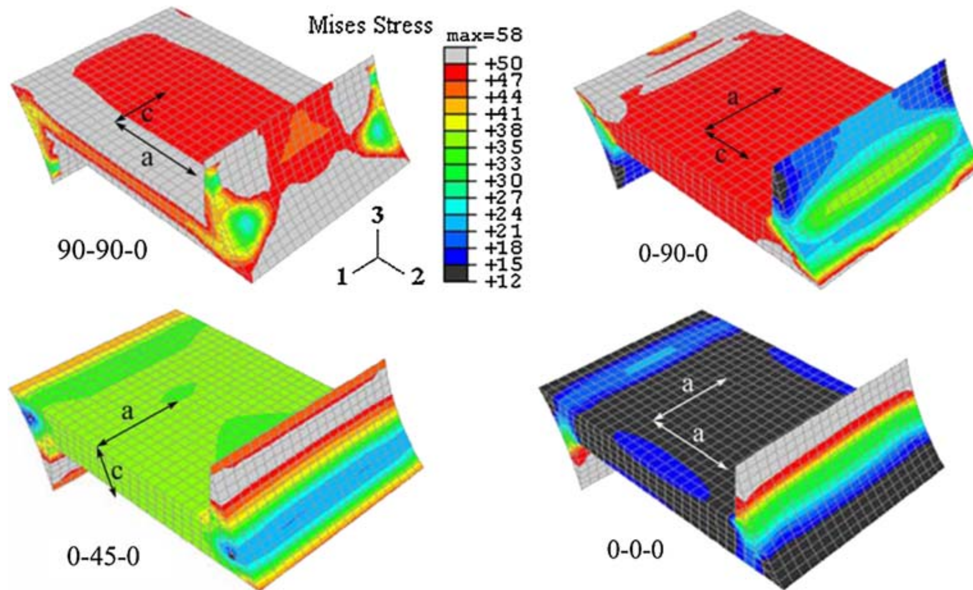

Fig. 6. von Mises stress distribution (MPa) in the shear lap model with different tin crystal orientations, showing widely varying locations of high stress with crystal orientation.

used with two cases: isotropic stiffness, as when a randomly textured polycrystal would be used as a substrate, and where the copper has (001)[100] orientation, which is close to the case where a (001) fiber texture results from electrodeposition. As is clear from Fig. 5 for all three tin crystal orientations used in this analysis, the internal energy is slightly lower for the model having isotropic properties, but this is insignificant compared with the effect of tin orientation. It is known that the copper texture affects the orientation and morphology of Cu_6Sn_5 that forms in the interface,[67] but from this analysis it is clear that elastic anisotropy of the substrate is not likely to have a large influence on the deformation of tin.

Spatial Distribution of Stress and Strain Energy

Figure 6 shows the von Mises stress distribution for the shear lap model and four different tin orientations. The fillet geometry in the shear lap model makes the deformation nonsymmetric in the x and y directions, and the effect of crystal orientation on stress in the fillet is dramatic; for a tin-based solder with 0–90–0 orientation, the von Mises stress is relatively small in the fillets where it is high for 90–90–0 orientation. However, for both 90–90–0 and 0–90–0 orientations, in which the c-axis of the crystal is parallel to the interface, the von Mises stress is high in most regions of the solder joint. The internal energy shown in Fig. 4 shows the highest value of internal energy for the 90–90–0 tin orientation. In contrast, the stresses (and total energy) for the 0–0–0 orientation are low in the substrate interface, and higher only in the regions of the fillet farthest from the joint interface, which would have little impact on damage generation in the joint. A tin-based solder with the 0–45–0 orientation shows a behavior between 0–90–0 and 0–0–0 orientations. Based on these observations one may conclude that tin-based solder with the 90–90–0 orientation is more susceptible to damage because the von Mises stress is high in almost all surface and interface regions of the solder joint.

Perhaps the most important components of the stress tensor are the shear stress components, as the differential expansion resulting from the c-axis $\parallel$ substrate interface imposes strong mode II shear displacements in interfaces. Among the shear stresses that develop, the largest values are commonly for the σ_{23} component. As shown in Fig. 7, the maximum shear stress for the 90–90–0 orientation is at the corners of, and beneath, the fillets. However, for the 0–90–0 and the 0–45–0 orientations, the largest σ_{23} stress locations may be a worse condition, where the shear is uniformly large at the lower edge of the fillet at the substrate interface, where cracks are often observed in similar geometries.[17] The σ_{23} shear is also very large for the 0–45–0 and 0–0–0 orientations under the upper fillet edge with the component (rather than the substrate).

Figures 8 and 9 show the von Mises stress and shear stress contours for the cylindrical geometry. The magnitude of the von Mises stress and shear stress in this case is in the same range as for the shear lap geometry. The distribution of the stresses and region where maxima are found are different in detail, but in both geometries, when the c-axis is in the plane of the substrate, the gradients of stress are greatest perpendicular to the c-axis. For all three orientations, the maximum von Mises stress

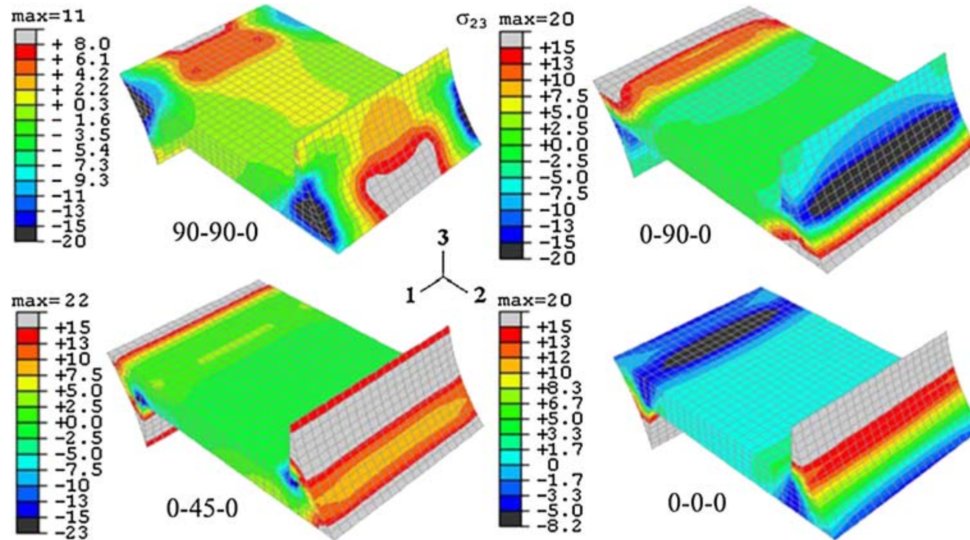

Fig. 7. Shear stress σ_{23} (MPa) in the shear lap model with different tin crystal orientations, showing varying shear stress distributions with crystal orientation. Other shear stress components have smaller values and are more uniform.

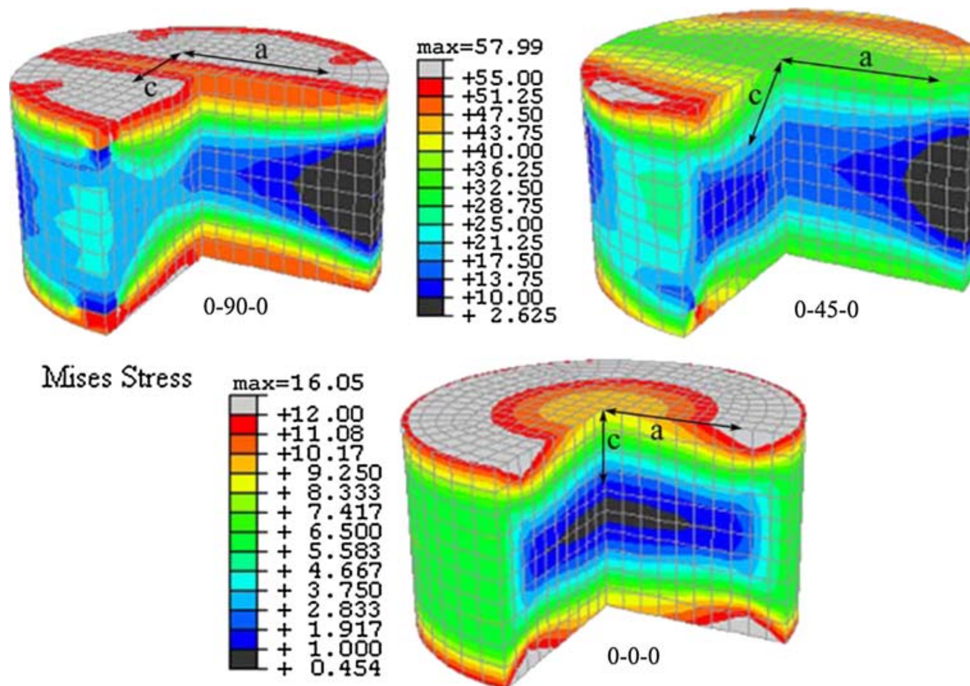

Fig. 8. von Mises stress (MPa) distribution in the cylindrical model; one-quarter is removed to reveal the stress state in the interior.

occurs at the tin–copper interface, which indicates that damage would probably nucleate in a region close to the interface, which is commonly observed experimentally and in other modeling efforts.[16–18,39]

Comparing the results of the cylindrical and the shear lap geometries, it is clear that the geometry of the joint has significant impact on the damage nucleation sites and the energy dissipated in tin. The shear lap geometry imposes more constraints on the joint for the volume of tin involved, and therefore requires more of the tin to deform to accommodate these constraints. Hence, the volume of tin with respect to the surface area constraints is much smaller for the shear lap geometry, resulting in 100 times greater dissipated energy (per unit mass) in the shear lap geometry (Figs. 4 and 5). In a real solder ball geometry, the concentration of strain in the interfacial region would be even greater than

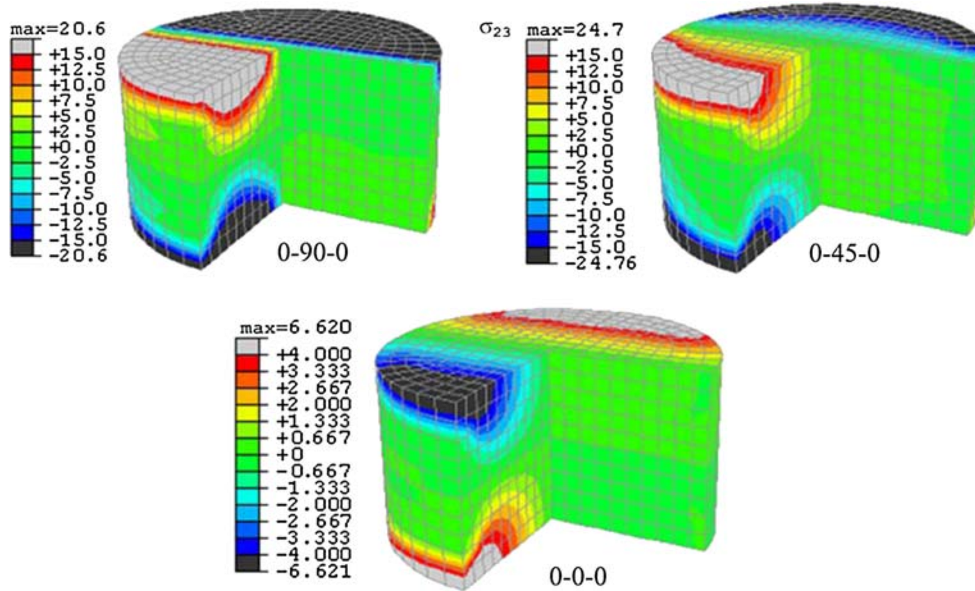

Fig. 9. Shear stress σ_{23} distribution for the cylindrical sample; one-quarter is removed to reveal stresses inside.

modeled, as the middle region would have even more volume to carry the same stresses; very little deformation takes place in the majority of the solder ball volume. In both geometries, the greatest stresses are observed in the interfacial regions, and are largest where the *c*-axis is in the interface. The concentration of stress near the interfaces is consistent with observations of strain concentrations and cracking that are commonly observed near the interface in solder ball joints. The fact that similar cracks are not uniformly observed in all joints is consistent with the strong effect of crystal orientation illustrated in these calculations.[49]

Based on the simulations and analysis above, one can easily see that the 0–0–0 Sn orientation would provide the lowest stress, and consequently the best reliability, in a tin-based solder joint. However, the von Mises stress may not be the best predictor of regions where damage is most likely to nucleate. From the point of view of fatigue, the location of maximum local plastic deformation may be a better way to predict a damage nucleation site. The local *plastic* work per unit volume was also plotted for all conditions, and for most tin orientations, such as the 0–45–0 and 0–90–0 orientations in the shear lap model, and the 0–45–0 orientation in the cylindrical model, the plastic deformation is largest where the von Mises stress has its highest values. However, for the 90–90–0 orientation in the shear lap model and 0–90–0 in cylindrical model, the von Mises stress is not as directly correlated to plastic deformation. Figure 10 shows the distribution of plastic work in these two orientations, from which it is clear that plastic deformation is more focused at its maximal location than the stress, and is concentrated in regions on the edges near the interface. Such localization cannot be inferred from the von Mises stress contours in Figs. 6 and 8. This result is also a consequence of a more sophisticated constitutive model that allows highly favored slip systems to operate preferentially when the resolved shear stress is high.

This analysis is much simpler than what is practically observed in real electronic packages, where additional boundary conditions must be imposed due to differential expansion effects between joined components; for example, highly localized strains dependent on crystal orientation were also observed in the crystal plasticity modeling of Gong et al.[39] They incorporated stress relaxation capability into their material model, as well as the effects of component-substrate differential expansion as an evolving boundary condition on the solder joint, which simulated the thermal cycling conditions realistically. However, they did not incorporate the elastic and thermal expansion anisotropy that is investigated herein. Despite the simplifications in the present work, the results are consistent with observations of cracks occurring preferentially in joints where the *c*-axis is nearly in the plane of the substrate that are discussed in detail in Ref. 49. This work shows that anisotropic finite element crystal plasticity modeling can at least qualitatively predict orientations that are problematic for reliability of lead-free solder joints. Combining the features of the modeling in the present paper with the features in the modeling approach of Gong et al. will lead to more credible material modeling that will improve the ability to quantitatively predict the reliability of lead-free solder joints in the future. With such a model, it will become possible to also identify conditions that will lead to driving forces for minimizing elastic strain energy by grain boundary migration,[47] or localized recrystallization due to

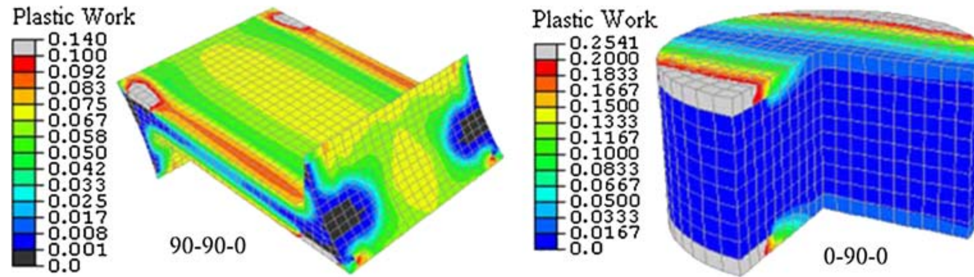

Fig. 10. Plastic work per unit volume (MPa/mm^3) contours for the {90,90,0} orientation in the shear lap model and {0,90,0} orientation in the cylindrical model.

strain concentrations when multiple crystal orientations are used in the initial joint geometry.[68–71]

CONCLUSION

The crystal orientation of the tin-based solder has a dominant effect on stress and strain (and hence, on probable damage nucleation) in lead-free tin-based solder joints. For the case of thermomechanical fatigue of solder joints in which only intrinsic thermal loads are present, a tin crystal orientation that puts the *c*-axis of the crystal in the direction that is less constrained leads to smaller stresses and lower internal energy, which would provide better reliability of the solder joint. In contrast, when the *c*-axis is in the plane of the substrate, large stresses develop in the interfaces that have large shear components that would facilitate a mode II crack nucleation condition. Despite simplifying assumptions, the results are qualitatively consistent with observed orientations that developed damage in thermally cycled physical packages.[49]

The texture of the copper substrate may be different due to different processing parameters or anisotropic effects of layers beneath the copper. However, the elastic effects of copper texture (and hence, preferred orientations in the intermetallic layer) do not have a significant effect on deformation in tin-based solder joints.

REFERENCES

1. M. Kerr and N. Chawla, *Acta Mater.* 52, 4527 (2004).
2. F. Guo, S. Choi, K.N. Subramanian, T.R. Bieler, J.P. Lucas, A. Achari, and M. Paruchuri, *Mater. Sci. Eng. A* 351, 190 (2003).
3. S. Choi, J. Lee, F. Guo, T.R. Bieler, K.N. Subramanian, and J.P. Lucas, *JOM* 53, 22 (2001).
4. C.M.L. Wu, D.Q. Yu, C.M.T. Law, and L.R. Wang, *Mater. Sci. Eng. R* 44, 1 (2004).
5. M. Amagai, M. Watanabe, M. Omiya, K. Kishimoto, and T. Shibuya, *Microelectron. Reliab.* 42, 951 (2002).
6. A.U. Telang, T.R. Bieler, D.E. Mason, and K.N. Subramanian, *J. Electron. Mater.* 32, 1455 (2003).
7. I.E. Anderson and J.L. Harringa, *J. Electron. Mater.* 33, 1485 (2004).
8. Y. Zhao, Y. Miyashita, and Y. Mutoh, *Int. J. Fatigue* 23, 723 (2001).
9. J.W. Yoon and S.B. Jung, *J. Mater. Sci.* 39, 4211 (2004).
10. S. Terashima and M. Tanaka, *Mater. Trans.* 45, 681 (2004).
11. C. Kanchanomai and Y. Mutoh, *Mater. Sci. Eng. A* 381, 113 (2004).
12. Q.L. Zeng, Z.G. Wang, A.P. Xian, and J.K. Shang, *J. Electron. Mater.* 34, 62 (2005).
13. J.G. Lee, F. Guo, S. Choi, K.N. Subramanian, T.R. Bieler, and J.P. Lucas, *J. Electron. Mater.* 31, 946 (2002).
14. H. Kato, K. Matsubara, and K. Kageyama, *Mater. Sci. Technol.* 19, 1403 (2003).
15. S. Terashima, Y. Kariya, T. Hosoi, and M.J. Tanaka, *Electron. Mater.* 32, 1527 (2003).
16. Y.-L. Shen, N. Chawla, E.S. Ege, and X. Deng, *Acta Mater.* 53, 2633 (2005).
17. M. Ahmad, K. Hubbard, and M. Hu, *J. Electron. Packag.* 127, 290 (2005).
18. R.S. Sidhu and N. Chawla, *Metall. Mater. Trans.* 39A, 799 (2008).
19. H. Ye, C. Basaran, and D.C. Hopkins, *Int. J. Damage Mech.* 15, 41 (2006).
20. W. Dreyer and W.H. Muller, *Int. J. Solids Struct.* 38, 1433 (2001).
21. T.Y. Lee, K.N. Tu, S.M. Kuo, and D.R. Frear, *J. Appl. Phys.* 90, 4502 (2001).
22. R. Darveaux, *Design and Reliability of Solders and Solder Interconnections* (Warrendale, PA: TMS, 1997), pp. 213–218.
23. H. Solomon, *ASME J. Electron. Pack.*, 113 (1991).
24. S.K. Kang, D.Y. Shih, D. Leonard, D.W. Henderson, T. Gosselin, S.I. Cho, J. Yu, and W.K. Choi, *JOM* 56, 34 (2004).
25. H.Y. Lu, H. Balkan, and K.Y.S. Ng, *J. Mater. Sci: Mater. Electron.* 17, 171 (2006).
26. Y. Takaku, X.J. Liu, I. Ohnuma, R. Kainuma, and K. Ishida, *Mater. Trans.* 45, 646 (2004).
27. M. He, Z. Chen, G.J. Qi, C.C. Wong, and S.G. Mhaisalkar, *Thin Solid Films* 462, 363 (2004).
28. F. Ochoa, X. Deng, and N. Chawla, *J. Electron. Mater.* 33, 1596 (2004).
29. K.J. Lau, C.Y. Tang, P.C. Tse, C.L. Chow, S.P. Ng, C.P. Tsui, and B. Rao, *Int. J. Fracture* 130, 617 (2004).
30. S. Choi, J.G. Lee, K.N. Subramanian, J.P. Lucas, and T.R. Bieler, *J. Electron. Mater.* 31, 292 (2002).
31. F. Guo, J.P. Lucas, and K.N. Subramanian, *J. Mater. Sci.: Mater. Electron.* 12, 27 (2001).
32. J.G. Lee and K.N. Subramanian, *Solder. Surf. Mt. Technol.* 17, 33 (2005).
33. J.G. Lee, A.U. Telang, T.R. Bieler, and K.N. Subramanian, *J. Electron. Mater.* 31, 11 (2002).
34. A.U. Telang and T.R. Bieler, *Scripta Mater.* 52, 1027 (2005).
35. H. Rhee, J.P. Lucas, and K.N. Subramanian, *J. Mater. Sci.: Mater. Electron.* 13, 477 (2002).
36. F. Yang and Li. JCM, *J. Mater. Sci: Mater. Electron.* 18, 191 (2007).
37. R.L.J.M. Ubachs, P.J.G. Schreurs, and M.G.D. Geers, *J. Mech. Phys. Solids* 52, 1763 (2004).
38. R.L.J.M. Ubachs, P.J.G. Schreurs, and M.G.D. Geers, *Mech. Mater.* 39, 685 (2007).

39. J. Gong, C. Liu, P.P. Conway, and V.V. Silberschmidt, *Comput. Mater. Sci.* 39, 187 (2007).
40. A.U. Telang and T.R. Bieler, *JOM* 57, 44 (2005).
41. A.U. Telang, T.R. Bieler, and M.A. Crimp, *Mater. Sci. Eng. A* 421, 22 (2006).
42. A.U. Telang, T.R. Bieler, S. Choi, and K.N. Subramanian, *J. Mater. Res.* 17, 2294 (2002).
43. A.U. Telang and T.R. Bieler, *JOM* 57, 44 (2005).
44. S. Park, R. Dhakal, L. Lehman, and E.J. Cotts, *Acta Mater.* 55, 3253 (2007).
45. S. Park, R. Dhakal, L. Lehman, and E.J. Cotts, *IEEE Trans. Compon. Pack. Technol.* 30, 178 (2007).
46. L.P. Lehman, S.N. Athavale, T.Z. Fullem, A.C. Giamis, R.K. Kinyanjui, M. Lowenstein, K. Mather, R. Patel, D. Rae, J. Wang, Y. Xing, L. Zavalij, P. Borgesen, and E.J. Cotts, *J. Electron.* 33, 1429 (2004).
47. A.U. Telang, T.R. Bieler, A. Zamiri, and F. Pourboghrat, *Acta Mater.* 55, 2265 (2007).
48. P. Borgesen, T. Bieler, L.P. Lehman, and E.J. Cotts, *MRS Bull.* 32, 360 (2007).
49. T.R. Bieler, H. Jiang, L.P. Lehman, T. Kirkpatrick, E.J. Cotts, and B. Nandagopal, *IEEE Trans. Compon. Packag. Technol.* 31, 370 (2008).
50. B. Duzgun, A.E. Ekinci, I. Karaman, and N. Ucar, *J. Mech. Behav. Mater.* 10, 187 (1999).
51. M. Fujiwara and T. Hirokawa, *J. Jpn. Inst. Metals* 51, 830 (1987).
52. I. Dutta, *J. Electron. Mater.* 32, 201 (2003).
53. P. Sharma and P. Dasgupta, *J. Electron. Pack. (Trans. ASME)* 124, 292 (2002).
54. Y. Wei, C.L. Chow, K.J. Lau, P. Vianco, and H.E. Fang, *J. Electron. Packag.* 126, 367 (2004).
55. T.R. Bieler and T.K. Lee, Unpublished research.
56. J.R. Mayeur and D.L. McDowell, *Int. J. Plast.* 23, 457 (2007).
57. G. Venkatramani, S. Ghosh, and M. Mills, *Acta Mater.* 55, 3971 (2007).
58. M. Werwer and A. Cornec, *Int. J. Plast.* 22, 1683 (2006).
59. D. Kumar, T.R. Bieler, P. Eisenlohr, D.E. Mason, M.A. Crimp, F. Roters, and D. Raabe, *J. Eng. Mater. Technol. Trans. ASME* 130, 021012 (2008).
60. D.G. House and E.V. Vernon, *Br. J. Appl. Phys.* 11, 254 (1960).
61. V.T. Desphande and D.B. Sirdeshmukh, *Acta Cryst.* 15, 294 (1962).
62. A. Zamiri (Ph.D. Thesis, Michigan State University, 2008).
63. *ABAQUS Manual, Version 6.3* (Providence, RI: Hibbit, Karlsson & Sorensen Inc., 2001).
64. J.W. Hutchison, *Proc. R. Soc. Lond. A* 319, 247 (1976).
65. Y.W. Chang and R.J. Asaro, *Acta Metall.* 29, 241 (1981).
66. D. Peirce, R. Asaro, and A. Needleman, *Acta Metall.* 30, 1087 (1982).
67. J.O. Suh, K.N. Tu, and N. Tamura, *J. Appl. Phys.* 102, 063511 (2007).
68. J.J. Sundelin, S.T. Nurmi, and T.K. Lepisto, *Mater. Sci. Eng. A* 474, 201 (2008).
69. J. Sylvestre and A. Blander, *J. Electron. Mater.* 37, 1618 (2008).
70. T. Laurila, T. Mattila, V. Vuorinen, J. Karppinen, M. Sippola, and J.K. Kivilahti, *Microelectron. Reliab.* 47, 1135 (2007).
71. D.W. Henderson, J.J. Woods, T.A. Gosselin, J. Bartelo, D.E. King, T.M. Korhonen, M.A. Korhonen, L.P. Lehman, S.K. Kang, P. Lauro, D.Y. Shih, C. Goldsmith, and K.J. Puttlitz, *J. Mater. Res.* 19, 1608 (2004).